INTERNATIONAL JOURNAL OF CLIMATOLOGY
Int. J. Climatol. **37**: 4043–4052 (2017)
Published online 28 February 2017 in Wiley Online Library
(wileyonlinelibrary.com) DOI: 10.1002/joc.4992

RMetS
Royal Meteorological Society

Characteristics of cloud cluster over the steep southern slopes of the Himalayas observed by CloudSat

Yilun Chen, Yunfei Fu,* Tao Xian and Xiao Pan

School of Earth and Space Sciences, University of Science and Technology of China, Hefei, China

ABSTRACT: A cloud cluster (CC) dataset is presented using CloudSat Cloud Profile Radar (CPR) observations from June to August, between 2006 and 2010. The CCs were defined by grouping contiguous cloud pixels using a defined criteria, including reflectivity, 'cloud mask', and topographic information. The characteristics of identified CCs were then analysed. Based on the complex topography of the southern Himalayas, four adjacent regions were selected, including the flat Gangetic Plains (FGP), the foothills of the Himalayas (FHH), the steep slope of the southern Himalayas (SSSH), and the Himalayan-Tibetan Plateau (HTPT). The characteristics of the CCs in the four regions were different, and the distribution of the cloud-top height gradually changed from bimodal (3 and 15 km) over the FGP and FHH, to unimodal (7–9 km) over the HTPT. From the plain to the Plateau, the average cloud-top height and cloud-base height increased after an initial decrease. The maximum reflectivity increased from −6 (plain) to 2 dBZ (slope areas), and then decreased to −2 dBZ (Plateau), which suggests that the CCs may produce precipitation on the slope. Maximum CCs occurred over the FHH. The characteristics of the CCs also showed semidiurnal variation, which may have been affected by the variation of the monsoon and the circulation over the mountain valley. According to the physical principles of the cloud-type definitions from ISCCP, high-level cirrus, deep convective CCs, and mid- to low-level CCs were categorized. As the elevation increased, the cloud-top height of the mid- to low-level CCs also significantly increased to 8 km, whereas the cloud-top height of the high-level cirrus clouds decreased. Our results suggest that the different characteristics of CCs may be caused by a strong upward motion interacting with the terrain of the Himalayas.

KEY WORDS cloud cluster; Himalayas; CloudSat; topography

Received 3 August 2016; Revised 8 December 2016; Accepted 12 December 2016

1. Introduction

The Tibetan Plateau, known as the Third Pole, is the highest plateau in the world with an average elevation above 4 km (Qiu, 2008). The latent and sensible heat over the Tibetan Plateau play a significant role on the weather and climate in the Asian monsoon region, even globally (Wu and Zhang, 1998; Liu and Chen, 2000; Wu *et al.*, 2007; Xu *et al.*, 2008, 2013; Zhong *et al.*, 2011; Zhu *et al.*, 2015). As a strong heat source in the summer, it is thought that the Tibetan Plateau controls the Asian summer monsoon systems through thermal forcing (Liu *et al.*, 2007; Wu *et al.*, 2012).

Clouds form precipitation and affect the latent heat over the Tibetan Plateau, providing significant radiative forcing on the earth-atmosphere system (Liou, 1986; Rossow and Schiffer, 1999). Different types and spatial distributions of clouds will produce different degrees of radiative forcing and precipitation (Wetherald and Manabe, 1988; Rosenfeld *et al.*, 2007, 2012). As a 'heat driving air pump' in summer, vigorous mesoscale convection over the Tibetan Plateau produces a large number of deep convection clouds, and transports water vapour and energy into the upper troposphere (Wu *et al.*, 2007; Yin *et al.*, 2009; Luo *et al.*, 2011; Qie *et al.*, 2014; Xian and Fu, 2015). Therefore, further knowledge of the thermal and dynamic effects of the Tibetan Plateau is dependent on an improved understanding of the cloud characteristics.

The launch of the CloudSat Cloud Profile Radar (CPR) provides a unique opportunity to observe three-dimensional cloud structures to comprehensively understand cloud characteristics (Stephens *et al.*, 2002; Im *et al.*, 2005). Sassen and Wang (2008) showed that the height-resolved CloudSat data can provide significantly enhanced insight into the global cloud system. Riley and Mapes (2009) focused on the vertical distribution of CloudSat echo tops and found that two main peaks at 2 and 14 km were associated with low and high clouds in the tropics, respectively. Between the main peaks, two distinct mid-level peaks were located in the 5–6 km and 7–8 km layers. Bacmeister and Stephens (2011) analysed the spatial characteristics of cloud objects derived using CloudSat data, and defined some indexes for statistics.

The cloud structure also shows regional differences over the Tibetan Plateau and the adjacent regions. Barros *et al.* (2004) found that the clouds and rainfall over the southern Himalayas are influenced by the topography at various spatial scales ranging from 1 to 5 km up to continental-scale. Fu *et al.* (2006) revealed a 'tower mast'

* Correspondence to: Y. Fu, School of Earth and Space Sciences, University of Science and Technology of China, Hefei, Anhui 230026, China.
E-mail: fyf@ustc.edu.cn

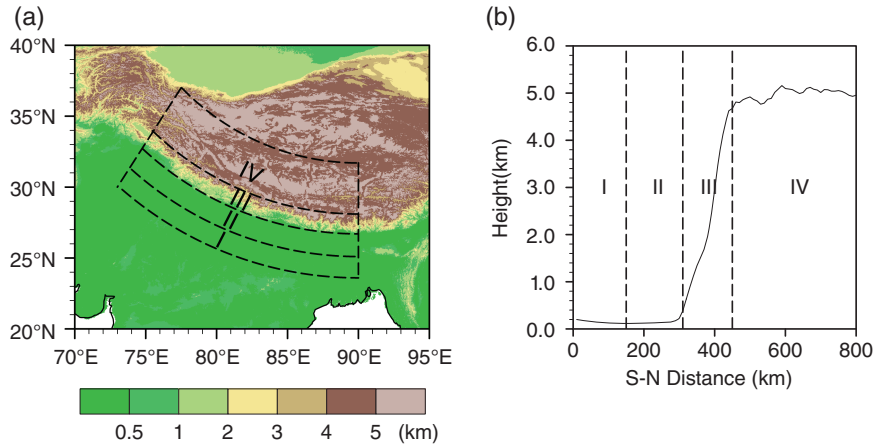

Figure 1. (a) The distributions of elevations and (b) the elevations from south (S) to north (N) in the radial cross-section of the study regions. Regions I, II, III, and IV represent the flat Gangetic Plains (FGP), the foothills of the Himalayas (FHH), the steep slope of the southern Himalayas (SSSH), and the Himalayan-Tibetan Plateau tableland (HTPT), respectively.

shape of precipitation over the Tibetan Plateau and found that there were more isolated rain cells with strong convection over the Plateau than its nearby regions. Houze *et al.* (2007) examined the three-dimensional structure of the summer monsoon convection in the Himalayas, and found that steep topography enhanced the formation and longevity of the broad stratiform echoes. Luo *et al.* (2011) produced schematics of the convection over the Tibetan Plateau and the adjacent regions using CloudSat/CALIPSO data, and revealed that the deep convection over the Tibetan Plateau is shallower and less frequent. Fu *et al.* (2016; personal communication) identified that the highest rain frequency occurs over the slopes, with the largest rain rate taking place over the foothills.

A better understanding of the cloud characteristics over the steep southern slopes of the Himalayas is extremely important for the energy exchange between the Plateau and the southern plains. However, we only know some of the characteristics of cloud clusters (CCs) in this special terrain, which is not enough to understand the thermal and dynamic effect of the Tibetan Plateau. In addition, previous studies have been limited to only the qualitative analysis. In this study, by using CloudSat data from 2006 to 2010, an event-based method was applied to construct a CC dataset to address the following points more quantitatively. We wanted to understand the relationship between the cloud characteristics and topography. In particular, what the distributions of the characteristics of the CCs over the plain, foothills, slopes, and mountain top were. How the topography affects the vertical structure of CCs, and whether criteria can be formulated for the cloud-type definitions over the Tibetan Plateau and the adjacent regions using CloudSat data.

2. Data and methods

2.1. CloudSat CPR data

The standard product 2B-GEOPROF derived from CPR for June–August between 2006 and 2010, was used in this study. It provides cloud geometric profiles, including cloud mask and reflectivity (minimum detectable reflectivity range of −29.9 to −30.9 dBZ), and geolocation information (longitude, latitude, and elevation). A CloudSat profile was generated every 1.1 km along the orbit track, producing 125 samples in each profile with a resolution of 240 m (Sassen and Wang, 2008). As a member of the A-Train constellation, CloudSat uses a sun-synchronous 705-km-altitude orbit with 1330 and 0130 LST (Local Standard Time = UTC+Longitude/15) crossings of the equator (Stephens *et al.*, 2002, 2008).

2.2. Methods

Considering the complex terrain over the steepest slopes of the Himalayas, four regions were selected according to the topography (Figure 1(a)). Compared with the study regions chosen by Luo *et al.* (2011) and Qie *et al.* (2014), we selected smaller belts that were almost parallel to the steepest slope, which will effectively show the impacts of topography on clouds in the regions. In addition, the elevation trend in Figure 1(b) shows that the regions selected by our curved lines match the average topography of the Himalayas. Specifically, regions I and II represent the flat Gangetic Plains (FGP) and the foothills of the Himalayas (FHH), respectively, with elevations less than 0.5 km and standard deviations less than 0.2 km. Although the elevations were similar in region I and II, the distance to the Plateau led to their different circulation patterns. Region III was located on the steepest slope of the southern Himalayas (SSSH), with altitude rapidly varying from 0.5 to 5 km. The Himalayan-Tibetan Plateau tableland (HTPT, region IV) had the elevations greater than 4 km and a gentler slope than region III. Fu *et al.* (2016; personal communication) calculated the topography index and surface wind over these four regions. They suggested that the southwesterly flow from the Arabian Sea and the southerly flow from Bay of Bengal are blocked by the steep Himalayas, and turn northwest along the FHH with a low speed, forming a cyclonic gyre over Bangladesh (the eastern section of FGP and FHH).

Previous studies generally summarize the orbital observations into horizontal grids to count their spatial distributions. However, gridded averaged data loses original information, and cannot be used to study individual events. Furthermore, it is difficult to quickly search information for individual events from original data because of the large amount of information. Therefore, it was necessary to eliminate unnecessary data and establish a new CC dataset. The cloud-event-based method groups 'cloud' pixels and then assumes that these pixels form an individual CC (Zhang *et al.*, 2010, 2014; Bacmeister and Stephens, 2011; Luo *et al.*, 2011; Igel *et al.*, 2014).

CCs are defined by grouping 'cloud' pixels with reflectivity not less than −29 dBZ and cloud mask greater than or equal to 20. The 'cloud mask' contains values between 0 and 40, and increasing values indicate a reduced probability of a false detection. For example, 5% false detection was estimated via a CALIPSO comparison with a cloud mask of 20 (Marchand *et al.*, 2008). Only 'cloud' pixels greater than elevations of 1 km or more were used to avoid the influence caused by strong reflection from the land surface. The number of continuous 'cloud' pixels should be greater than or equal to 10 to diminish the partial-filling effect of small CCs. The geometric center of the CC was defined as its location. Based on these constraints, a CC dataset with topographic information was generated. Figure 2 shows the process of CloudSat detection and the CC identified by our criteria. The scanning orbit is shown in Figure 2(a), which scans over the four study regions continuously. Figure 2(b) shows the reflectivity provided by CPR 2B-GEOPROF. The reflectivity was greater than 10 dBZ at the surface. There should be a convective cloud above the surface with a strong echo that connects with the surface echo. An anvil accompanied by convection occurred at 29.5 N at 9–12 km height. The CCs identified by our criteria are shown in Figure 2(c) after eliminating the surface and no-cloud echoes. It is clear that a deep convective CC was located at the slopes and there were also some small CCs to the north.

Based on the criteria to identify CCs, some parameters were defined and calculated based on Bacmeister and Stephens (2011). Taking the largest CC in Figure 2(c) as an example, the definitions of the parameters are shown in Figure 3. Ht and Hb were the highest and lowest pixels in the CC, which were considered as the cloud-top and cloud-base heights, respectively. D was the maximum thickness of the CC; D = Ht − Hb. The maximum horizontal length Lmax was determined using the distance between the first and last pixels in each CC. In addition, some other parameters were defined based on reflectivity: Zmax (maximum reflectivity of the CC), Zav (average reflectivity of the CC) and S (cross-sectional area of the CC). Based on the physical properties of the CC, the average reflectivity profile was calculated by averaging the reflectivity layer-by-layer.

Before performing statistical analysis, the number of valid samples was calculated. Table 1 shows the populations of CCs both in the daytime and nighttime over the four study regions (total profiles detected by CloudSat are

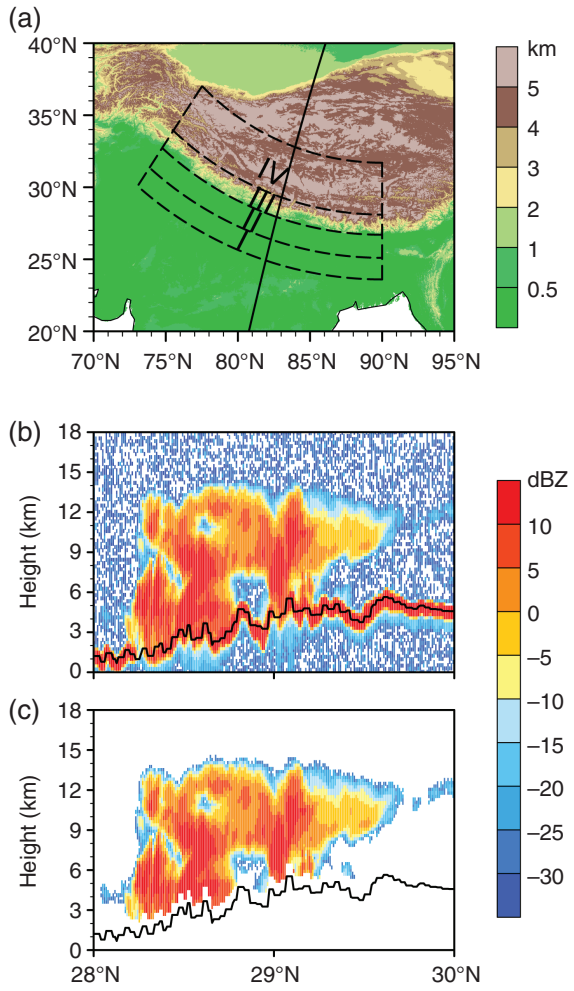

Figure 2. An example of identifying CCs. (a) An orbit scanned over the study regions on 23 June 2006 (Orbit 00802). (b) Radar reflectivity data with a latitude range from 28 to 30 N. (c) CCs identified by our criteria.

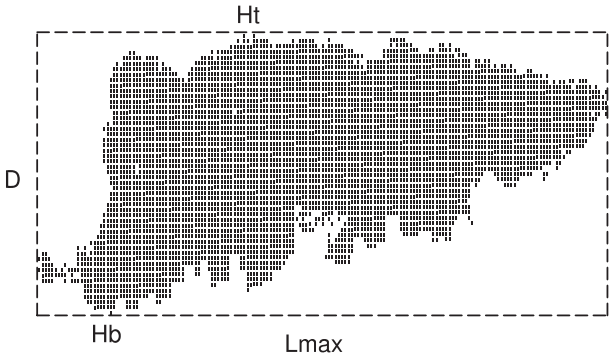

Figure 3. Close-up of the largest CC in Figure 2(c).

in brackets). In general, the total profiles of the daytime and nighttime were similar, with a difference of less than 10%. The populations of CCs at 1330 LST were greater than those at 0130 LST, with a difference of 40% over the HTPT. The populations of CCs in the daytime and nighttime were all greater than 500 over each region. Therefore, the sample size was large enough for the following statistical analysis.

Table 1. The populations of CCs and total profiles detected by CloudSat.

Time	I	II	III	IV
1330 LST	835 (48 528)	814 (51 871)	1234 (43 812)	2078 (96 386)
0130 LST	707 (51 389)	693 (53 006)	994 (39 535)	1469 (101 224)

3. Results

The probability distribution functions (PDFs) of four CCs' parameters are shown in Figure 4. Ht is distributed in two main peaks at 3 and 15 km over the FGP and FHH, respectively (Figure 4(a)). This is consistent with Riley and Mapes (2009), who used CloudSat CPR data and found that the two main peaks in the tropics associated with the low and high clouds were due to the trade inversion and tropopause. The cloud-top height increased to 7 and 9 km over SSSH and HTPT respectively as a result of the lifting of airflow by elevation rise. The peak at the tropopause gradually weakened, or even disappeared, with the proportion decreasing from 20 to 10%. The PDFs decreased significantly as the S increased over the SSSH and HTPT. A peak occurred over the FGP and FHH when S ranged from 10 to 30 km^2. The distributions of Zmax were similar over the SSSH and HTPT with two peaks. One peak was explained as cirrus (stratus) with weak convection, and the other as a CC with strong convection. Compared with the HTPT, the proportion of convective CC over the SSSH was a little higher. This is consistent with the findings of Fu *et al.* (2016; personal communication) using the TRMM PR data, who found that the highest rain frequency over the steep slopes of the Himalayas was located at the SSSH. Over the FGP and FHH, the Zmax peak was negative, and a weaker peak was observed between 10 to 20 dBZ. There was no significant difference of Zav among the four regions, and all were presented as a single peak at −25 to −20 dBZ.

Figure 5 shows the PDFs of four CC parameters in the nighttime. Although the overall distribution of these parameters was similar to that of the daytime, there were some differences. Compared with the daytime, the height of the CCs near the tropopause decreases slightly over FGP and FHH, whereas their proportion increased by about 10%. S and Zav also decreased to a certain extent. Furthermore, the peak of Zmax at 10 to 20 dBZ almost disappeared with only a single peak located at −20 dBZ. The above results indicate that nighttime CCs over FGP and FHH were smaller but higher and with more cirrus than daytime CCs. Compared with daytime CCs, S and Zav were also smaller and weaker over SSSH and HTPT, whereas Zmax increased slightly. These semidiurnal variations may have been affected by the variability of the monsoon and mountain-valley circulations. Furthermore, it is more difficult to form a deep convective CC in the nighttime because of higher stability and weaker heating compared with daytime.

The contoured frequency by altitude diagram (CFAD) is a statistical method to display the vertical distribution of storm properties within two-dimensional coordinate (property *vs* height). This method has been widely used in previous studies to analyse the vertical structure over different regions (Yuter and Houze, 1995; Houze *et al.*, 2007). Fu *et al.* (2003) successfully designed an improved method (CRAD, Contoured Rainrate by Altitude Diagram) to reveal the averaged vertical structure of precipitation. In the present study, the average reflectivity profile was first calculated in terms of CC. The CFAD method was then used to understand the vertical structure of the reflectivity and clouds inclusive of all four study regions (Figure 6). To minimize noise, only CFAD bins with at least four samples were used in the calculation of CFADs in Figure 6.

There were significant differences among the CFAD of the four regions (Figure 6). Three statistically distinct regimes are shown over the FGP and FHH, i.e. a low level, a high level with frequency greater than 0.12%, and a mid-level near the freezing layer. The high level was located within Z values of −25 to −15 dBZ, whereas Z in the low level was spread evenly from −25 dBZ to 0 dBZ. The mid-layer had lower Z values ranging from −25 to −20 dBZ, which may have been produced by shallow CCs. The greatest reflectivity (10 dBZ) in the middle level resulted from the combination of large reflectivity from liquid cloud particles and overlying precipitating particles, which implies a deep convective cloud. This is consistent with the results of Bacmeister and Stephens (2011) where deep convective clouds formed similar curved outlines. Over the SSSH, two high-frequency levels were still observed. However, frequency in the high level clearly decreased, and the curved outline in the mid-level was wider than that over the FGP and FHH. This shows the various patterns and degrees of convective CCs over the SSSH. The high-frequency regime at the high level disappeared, while the low level frequency was at its greatest and reached up to 0.2% over the HTPT. The mid-level appeared absent over the HTPT; however, the height of the low level over the HTPT was in fact similar to the mid-level of FGP. This phenomenon indicates that the CCs in the low and freezing levels were combined by the lifting topography of the Tibetan Plateau. This characteristic may result in the possible misidentification of the rain type by TRMM PR over the Tibetan Plateau as suggested by Fu and Liu (2007).

Moreover, there was a slight difference between the daytime and nighttime CFADs, mainly in the increasing frequency at high level; about 0.2% over the FGP and 0.16% over the HTPT. Compared with the daytime CFADs, the frequency in the low level decreased significantly, and the frequency of the curved outline similarly decreased and even disappeared. This is consistent with Figures 4 and 5 where more cirrus CCs and weaker convective CCs appeared in the nighttime than daytime.

Understanding the relationship between the cloud characteristics and topography was one of the main objectives of this study. To examine the impact of topography on the

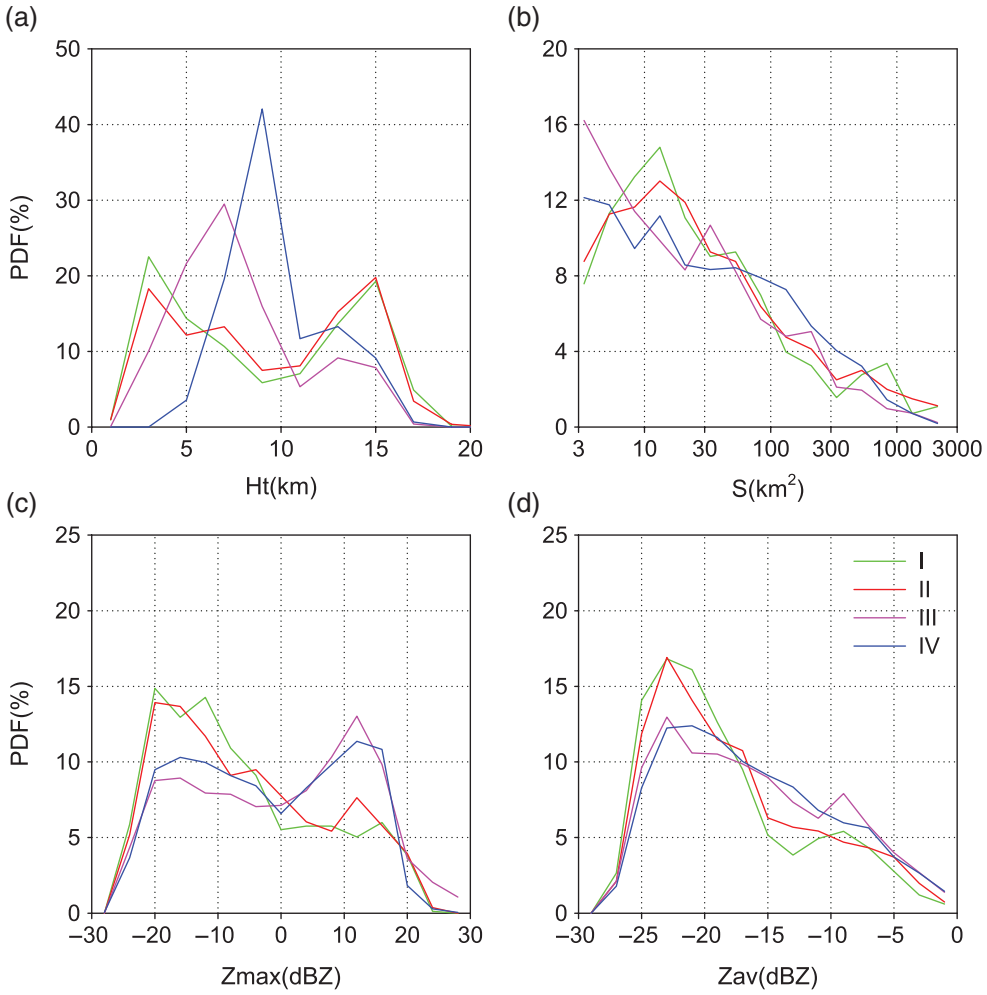

Figure 4. Probability distribution functions (PDFs) of the CC parameters at (a) 1330 LST Ht, (b) S, (c) Zmax, and (d) Zav.

variations of CC parameters, these parameters and elevations were averaged in the cross-section from the southern border of the FGP (Figure 7). Ht and Hb both showed a tendency to first decrease and then increase. In particular, Ht decreased from 9 km over the plains to less than 8 km over the SSSH, and then increased to 10 km over the HTPT. Hb ranged from 4.5 km over the SSSH to 7 km over the HTPT. Figure 7(a) also shows that the CC thickness was reduced by approximately 0.5 km from the plains to HTPT. Zmax increased from −6 dBZ over the FGP and FHH to 2dBZ over SSSH, and then decreased to −2 dBZ over the HTPT (Figure 7(b)). These changes were related to the flow of moist air masses, which was blocked by the steep Himalayas and then formed a low-level convergence zone with rain frequency peaks over the SSSH as suggested by Fu *et al.* (2016; personal communication). S peaked at FHH (180 km^2) and decreased rapidly to 90 km^2 over the SSSH. This may have resulted from the moisture content, which reduced as the elevation increased.

Figure 8 shows the impact of topography on the CC parameters in the nighttime. There were some consistent characteristics between daytime and nighttime, such as the Ht and Hb trends, reduced thinner thickness over the HTPT, and the Zmax peak over the SSSH. However, due to the thermal contrast, Ht in the nighttime was a little higher than that in the daytime over the FGP. Conversely, nighttime Ht was lower than daytime Ht over the HTPT. In the nighttime, the mountain-valley breezes reduced the uphill vapour transport, and the strong cooling over the Tibetan Plateau contributed to the weaker convection than that during daytime. This caused the drop in cloud-top height. The nighttime mid-level cold advection originated from the Plateau and the long-wave radiative cooling from the top of the cloud, and instability may have been triggered producing precipitation. The greatest Zmax in the nighttime over the SSSH may have been related to the late-night rainfall peak over the periphery of the Tibetan Plateau, as suggested by Yu *et al.* (2010).

Rossow and Schiffer (1999) produced cloud-type definitions using cloud top pressure and optical thickness for daytime, and cloud top pressure only for nighttime. However, due to the complex topography over the Tibetan Plateau and unavailable cloud optical thickness at night, it is difficult to compare the cloud characteristics between plains and mountains both in the daytime and nighttime. Based on the physical principles of the cloud-type definitions by Rossow and Schiffer (1999), CCs over the steep southern slopes of the Himalayas were categorized

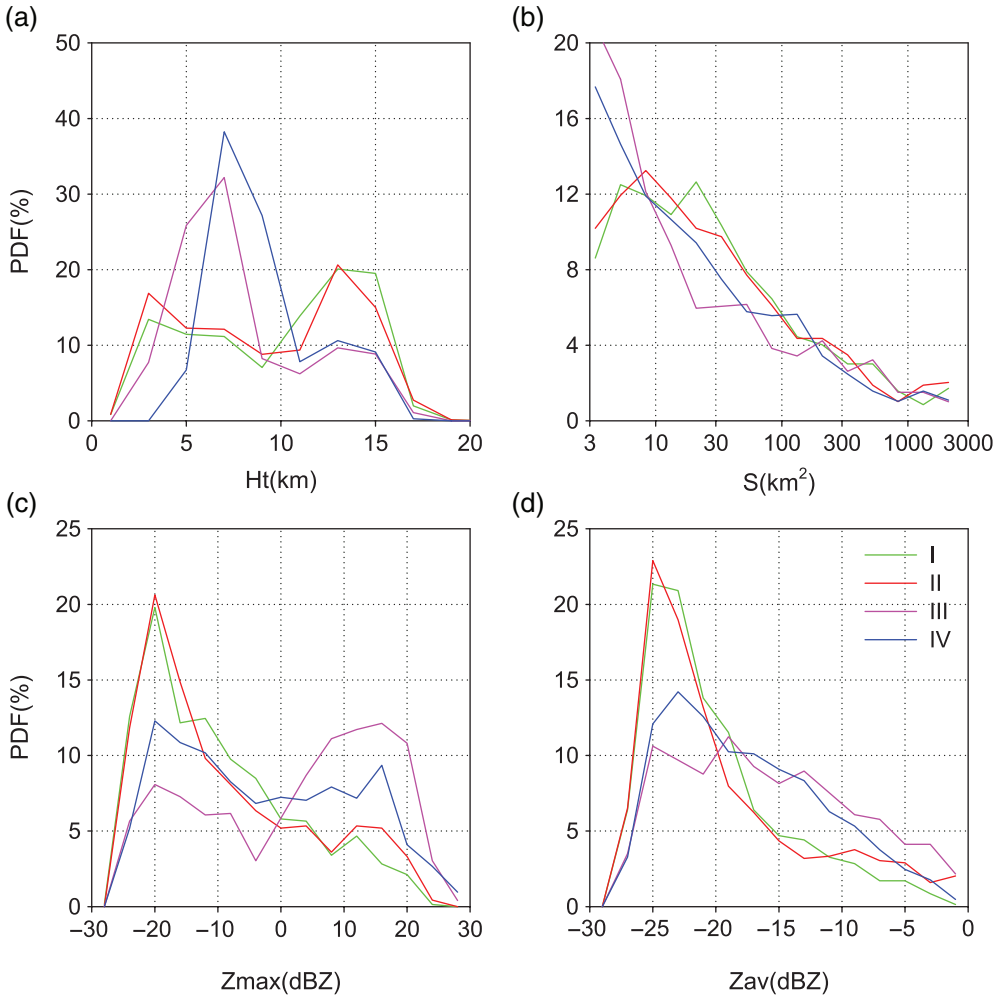

Figure 5. Similar to Figure 4, but for nighttime (0130 LST).

by the parameters defined in this study to investigate the change in CC parameters over the four study regions. Ht effectively represents the cloud-top information; Zmax is related to the cloud optical thickness to a certain extent; and S contains vertical and horizontal information. These three parameters were used to compare the CC characteristics over the different regions (Figure 9).

The three sections in Figure 9 were divided by the dashed black lines: high-level cirrus with Zmax less than 0 dBZ and Ht higher than 10 km; deep convective CCs with Zmax greater than 0 dBZ and Ht higher than 10 km; and mid to low-level CCs with Ht less than 10 km. The high-level cirrus were generally small and thin; the deep convective CCs were large and thick, and were likely able to penetrate the tropopause; and the mid- to low-level CCs contained nimbostratus with precipitation and strong Zmax, and small-scale cumulus. Figure 9 shows that the Ht of the mid- to low-level CCs clearly increased and reached 8 km as the elevation increased further up to HTPT. Conversely, the Ht of the high-level cirrus decreased by about 1 km and its proportions also reduced. The Ht of the mid- to low-level CCs increased as Zmax increased. At Zmax greater than 10 dBZ, the CCs showed significant vertical development where Ht increased markedly, and deep convective CCs formed and even penetrated the tropopause (17 km) (Xian and Fu, 2015). The differences between daytime and nighttime presented in Figure 9 were consistent with the above results.

4. Discussion and conclusion

Using observations of the CloudSat CPR for June–August, 2006–2010, a CC dataset was constructed and collocated with topographic information. Based on criteria to identify CCs, specific parameters were defined and calculated. This greatly increased the speed for search information of individual events, and specific types of CCs could be selected based on given regions or features.

Based on the dataset, the characteristics of the CCs over the steep southern slopes of the Himalayas and the adjacent regions in the daytime and nighttime were investigated to understand the topographic and thermodynamic effects on the characteristics of CCs during the monsoon season. The main results are summarized as follows.

The characteristics of the CCs in the FGP, FHH, SSSH, and HTPT were quite different. The distribution of cloud-top height gradually changed from bimodal (3 and 15 km) over the FGP and FHH, to unimodal (7–9 km) over

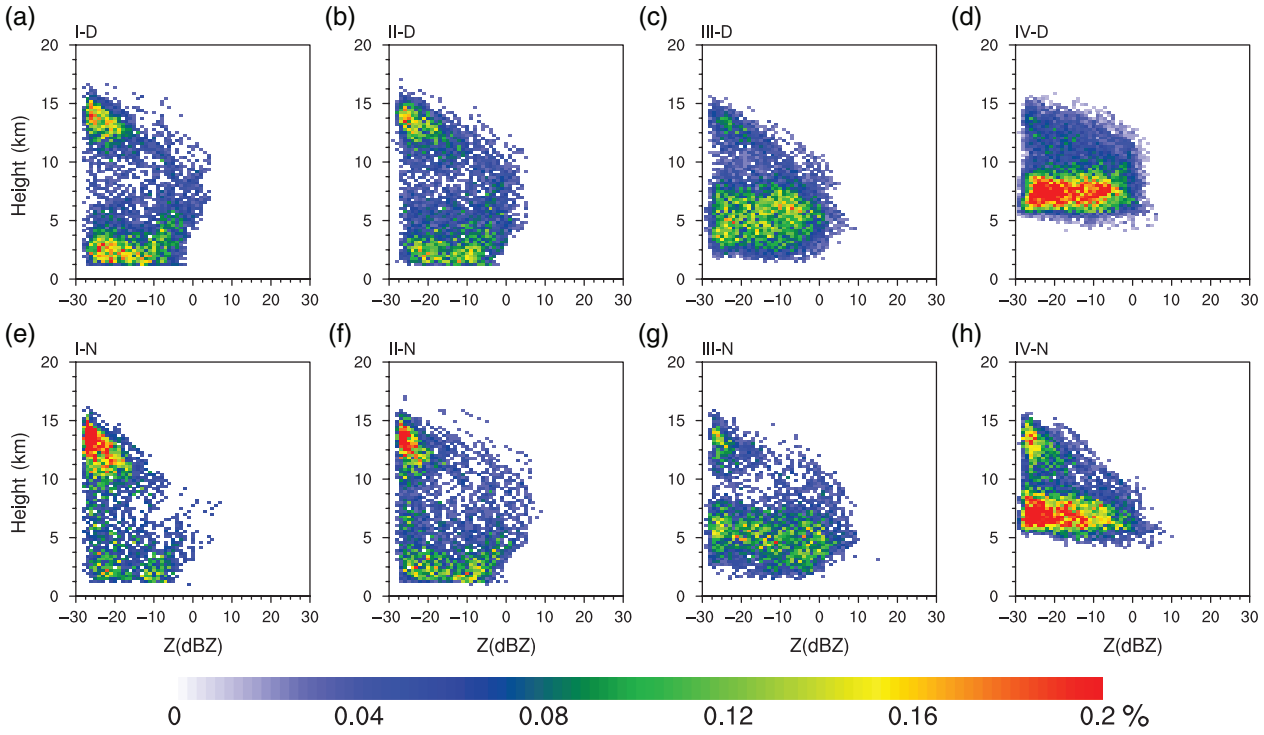

Figure 6. The Contoured Frequency by Altitude Diagrams (CFADs) of CCs over the four study regions. (a–d) 1330 LST, and (e–h) 0130 LST.

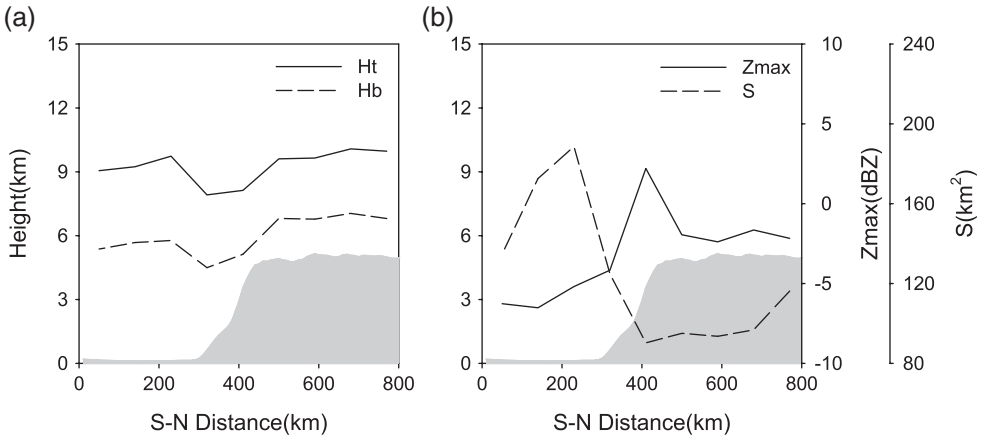

Figure 7. Variation of CCs' parameters with elevation from the south (S) to the north (N) in the cross-section of the study regions at 1330 (LST). (a) Ht and Hb, (b) Zmax and S.

the HTPT. There were two peaks of Zmax over the SSSH and HTPT; one for cirrus (stratus), and the other for strong convection, whereas only a single peak occured for cirrus (stratus) over the FGP and FHH. Two high-frequency regimes were shown in the CFADs over the FGP, FHH, and SSSH, whereas only a low-level regime existed over the HTPT, but with the highest frequency. In the cross-section from the southern plains to the Plateau, the average cloud-top and cloud-base heights both increased after an initial decrease as a result of mechanical lifting by the terrain in cloud production. Zmax increased from −6 (plain) to 2 dBZ (slope), and then decreased to −2 dBZ (Plateau), which suggests that the highest precipitation frequency occurred on the slopes. S peaked over the plains, and decreased rapidly over the SSSH.

CloudSat as a sun-synchronized orbit satellite, can obverse the semidiurnal variation of CCs. Nighttime CCs over FGP and FHH were smaller, higher and with more cirrus than daytime CCs. Nevertheless, Zmax increases slightly with the lower Ht over the SSSH compared with daytime. CFADs also showed that more cirrus CCs and less strong convective CCs appeared in the nighttime compared with daytime. This was related to the variation of the monsoon and the mountain-valley circulation. Higher stability and weaker heating than daytime also contributed to these results.

According to the physical principles of the cloud-type definitions from ISCCP, high-level cirrus, deep convective CCs, and mid- to low-level CCs were categorized by the characteristics of CCs. The Ht of the mid- to low-level

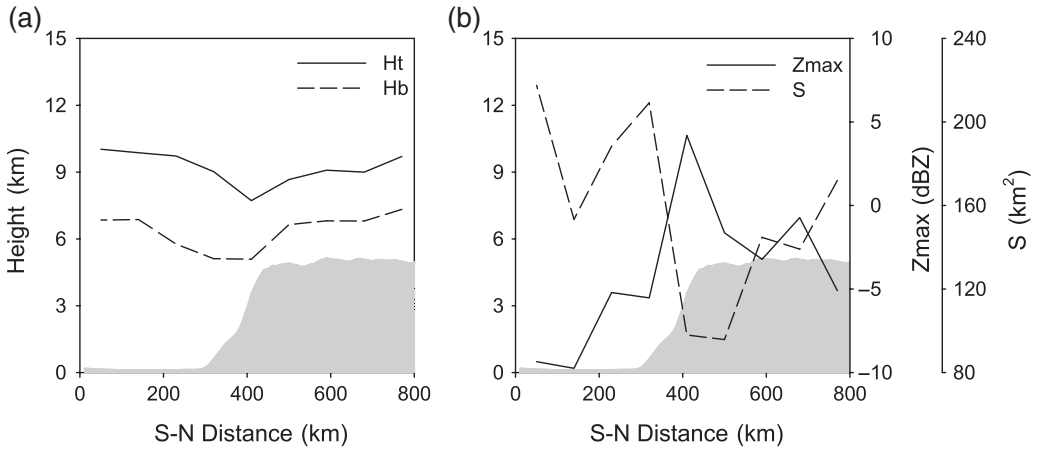

Figure 8. Same as Figure 7, but for nighttime (0130 LST).

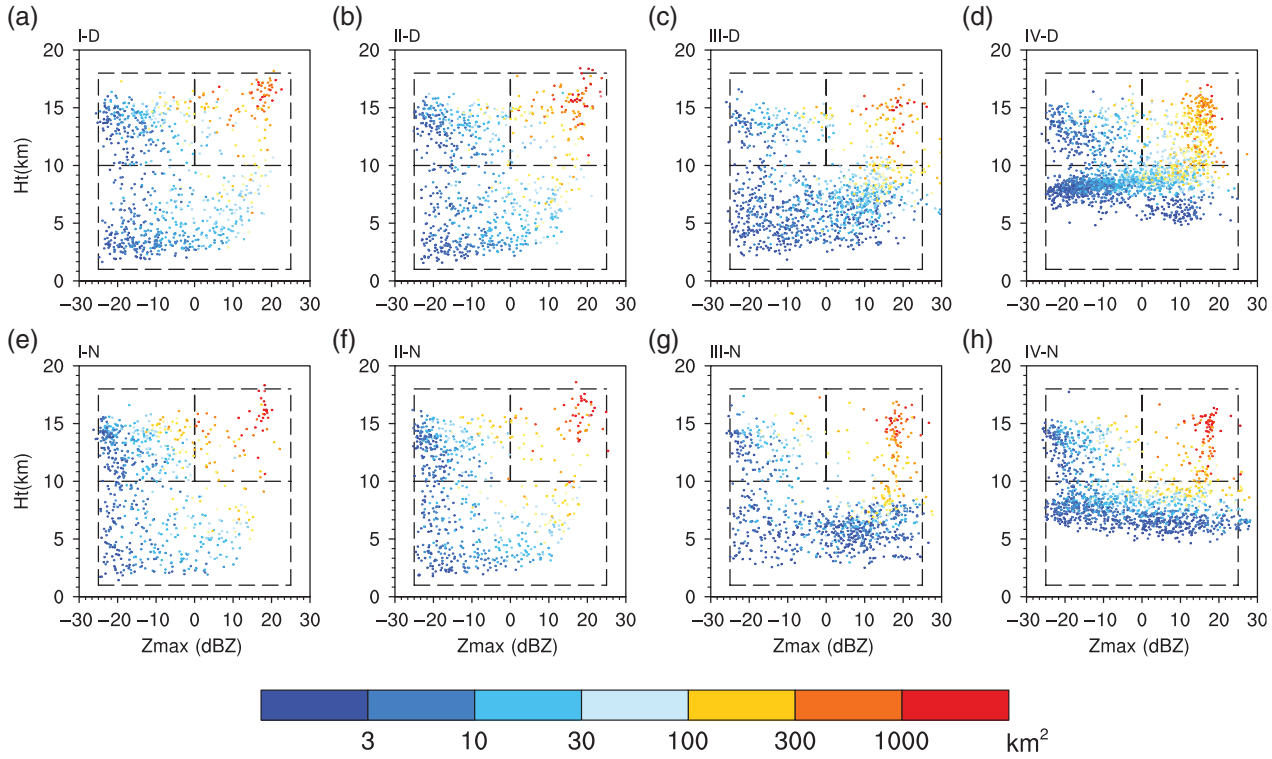

Figure 9. Relationship among the cloud-top height (Ht), maximum reflectivity (Zmax), and the cross-section (S) of the CC over the four study regions. (a–d) 1330 LST, and (e–h) 0130 LST.

CCs increased and reached 8 km as the elevation increased further, while the Ht and proportion of the high-level cirrus decreased.

Previous studies have illustrated convection over the Tibetan Plateau and the adjacent regions using schematic diagrams (Houze *et al.*, 2007; Luo *et al.*, 2011). A schematic diagram was developed (Figure 10) to visualize the structure of the CCs and their associated circulation in the four study areas. The South Asian monsoon brings southwesterly low-level air from the Arabian Sea and the Bay of Bengal to the Tibetan Plateau. Over the FGP and FHH, the cloud top of CCs was mainly distributed into two levels. After encountering the steep Himalayas, the low-level airflow with abundant moisture produced the highest rain frequency and Zmax over the SSSH due to the strong upward motion caused by topographic forcing and the 'heat driving air pump'. However, according to the moisture content, which reduced as elevation and the high rain frequency increased, the average cloud-top height appeared lower than that for the FHH, FGP, and HTPT. Owing to the lowest tropopause and highest elevation over the HTPT, the cloud top of the CCs displayed one peak, that is, the CCs were condensed by the topography. The South Asian High controls the high level of the Tibetan Plateau in boreal summer, and appears as convergence at the lower level and divergence at the higher level. The precipitation CCs dissipated to form cirrus CCs at the higher level, where the cloud top mainly depended on

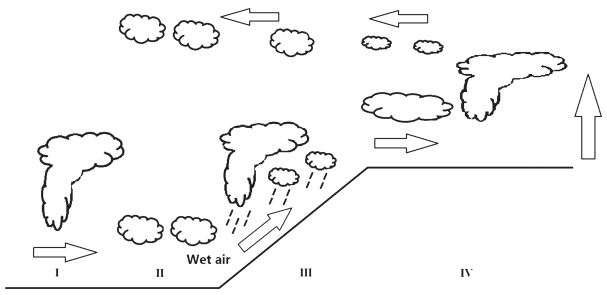

Figure 10. Schematic diagram of the distribution of CCs and the circulation along the radial direction from south to north in the study regions.

the height of the tropopause. As a result, the height of the cirrus CCs increased when the cirrus CCs moved to the FHH from the HTPT.

In this study, we suggested possible interaction mechanisms between the clouds and the terrain. These results are important to understand how the high mountain area of the Himalayas impacts regional and global climate. Clouds are an important indicator of the thermal and dynamic effects of the atmosphere and the land surface. This study provides observations of CC characteristics that have been changed by the terrain for cloud parameterization in future studies.

Some of the uncertainties and limitations of this study include the following. Because of the strong reflection from the land surface, the clouds close to the surface, in particular, may not have been identified by our criteria. Therefore, the average cloud-top height may have been lower than what was estimated in this paper. In addition, because Cloudsat is as a sun-synchronous satellite that crosses the equator at 1330 and 0130 LST, a full sample of the diurnal cycle was not available. Future use of the multi-satellite combination will reduce the bias of cloud identification, and further work using geostationary satellite data will be able to confirm the diurnal cycle.

Acknowledgements

This work is supported by the Third Tibetan Plateau Scientific Experiment: Observations for Boundary Layer and Troposphere (grant no. GYHY201406001), the National Natural Science Foundation of China (NSFC, grant no. 91337213, 41230419, and 41505033), the Special Funds for Public Welfare of China (grant no. GYHY201306077), Special Financial Grant from the China Postdoctoral Science Foundation (grant no. 2016T90572) and the Fundamental Research Funds for the Central Universities.

References

Bacmeister JT, Stephens GL. 2011. Spatial statistics of likely convective clouds in CloudSat data. *J. Geophys. Res. Atmos.* **116**: D04104.

Barros AP, KIM G, Williams E, Nesbitt SW. 2004. Probing orographic controls in the Himalayas during the monsoon using satellite imagery. *Nat. Hazards Earth Syst. Sci.* **4**: 29–51.

Fu YF, Liu GS. 2007. Possible misidentification of rain type by TRMM PR over Tibetan plateau. *J. Appl. Meteorol. Clim.* **46**: 667–672.

Fu YF, Lin YH, Liu GS, Wang Q. 2003. Seasonal characteristics of precipitation in 1998 over East Asia as derived from TRMM PR. *Adv. Atmos. Sci.* **20**: 511–529.

Fu YF, Liu GS, Wu GX, Yu RC, Xu YP, Wang Y, Li R, Liu Q. 2006. Tower mast of precipitation over the central Tibetan Plateau summer. *Geophys. Res. Lett.* **33**: L058025.

Houze RA, Wilton DC, Smull BF. 2007. Monsoon convection in the Himalayan region as seen by the TRMM precipitation radar. *Q. J. R. Meteorol. Soc.* **133**: 1389–1411.

Igel MR, Drager AJ, van den Heever SC. 2014. A CloudSat cloud object partitioning technique and assessment and integration of deep convective anvil sensitivities to sea surface temperature. *J. Geophys. Res. Atmos.* **119**: 17.

Im E, Wu CL, Durden SL. 2005. Cloud profiling radar for the CloudSat mission. *IEEE Aerosp. Electron. Syst. Mag.* **20**: 15–18.

Liou KN. 1986. Influence of cirrus clouds on weather and climate processes: a global perspective. *Mon. Weather Rev.* **114**: 1167–1199.

Liu XD, Chen BD. 2000. Climatic warming in the Tibetan Plateau during recent decades. *Int. J. Climatol.* **20**: 1729–1742.

Liu YM, Hoskins B, Blackburn M. 2007. Impact of Tibetan orography and heating on the summer flow over Asia. *J. Meteorol. Soc. Jpn.* **85B**: 1–19.

Luo YL, Zhang RH, Qian WM, Luo ZZ, Hu X. 2011. Intercomparison of deep convection over the Tibetan Plateau-Asian monsoon region and subtropical North America in Boreal summer using CloudSat/CALIPSO data. *J. Clim.* **24**: 2164–2177.

Marchand R, Mace GG, Ackerman T, Stephens G. 2008. Hydrometeor detection using Cloudsat: an earth-orbiting 94-GHz cloud radar. *J. Atmos. Oceanic Technol.* **25**: 519–533.

Qie XS, Wu XK, Yuan T, Bian JC, Lu DR. 2014. Comprehensive pattern of deep convective systems over the Tibetan Plateau-South Asian monsoon region based on TRMM Data. *J. Clim.* **27**: 6612–6626.

Qiu J. 2008. The third pole. *Nature* **454**: 393–396.

Riley EM, Mapes BE. 2009. Unexpected peak near-15 degrees C in CloudSat echo top climatology. *Geophys. Res. Lett.* **36**: L09819.

Rosenfeld D, Dai J, Yu X, Yao ZY, Xu XH, Yang X, Du CL. 2007. Inverse relations between amounts of air pollution and orographic precipitation. *Science* **315**: 1396–1398.

Rosenfeld D, Woodley WL, Khain A, Cotton WR, Carrio G, Ginis I, Golden JH. 2012. Aerosol effects on microstructure and intensity of tropical cyclones. *Bull. Am. Meteorol. Soc.* **93**: 987–1001.

Rossow WB, Schiffer RA. 1999. Advances in understanding clouds from ISCCP. *Bull. Am. Meteorol. Soc.* **80**: 2261–2287.

Sassen K, Wang Z. 2008. Classifying clouds around the globe with the CloudSat radar: 1-year of results. *Geophys. Res. Lett.* **35**: L048054.

Stephens GL, Vane DG, Boain RJ, Mace GG, Sassen K, Wang ZE, Illingworth AJ, O'connor EJ, Rossow WB, Durden SL, Miller SD, Austin RT, Benedetti A, Mitrescu C. 2002. The Cloudsat mission and the A-train: a new dimension of space-based observations of clouds and precipitation. *Bull. Am. Meteorol. Soc.* **83**: 1771–1790.

Stephens GL, Vane DG, Tanelli S, Im E, Durden S, Rokey M, Reinke D, Partain P, Mace GG, Austin R, L'ecuyer T, Haynes J, Lebsock M, Suzuki K, Waliser D, Wu D, Kay J, Gettelman A, Wang Z, Marchand R. 2008. CloudSat mission: Performance and early science after the first year of operation. *J. Geophys. Res. Atmos.* **113**: D00A18.

Wetherald RT, Manabe S. 1988. Cloud feedback processes in a general-circulation model. *J. Atmos. Sci.* **45**: 1397–1415.

Wu GX, Zhang YS. 1998. Tibetan Plateau forcing and the timing of the monsoon onset over South Asia and the South China Sea. *Mon. Weather. Rev.* **126**: 913–927.

Wu GX, Liu YM, Wang TM, Wan RJ, Liu X, Li WP, Wang ZZ, Zhang Q, Duan AM, Liang XY. 2007. The influence of mechanical and thermal forcing by the Tibetan Plateau on Asian climate. *J. Hydrometeorol.* **8**: 770–789.

Wu GX, Liu YM, He B, Bao Q, Duan AM, Jin FF. 2012. Thermal controls on the Asian summer monsoon. *Sci. Rep.* **2**: 404.

Xian T, Fu YF. 2015. Characteristics of tropopause-penetrating convection determined by TRMM and COSMIC GPS radio occultation measurements. *J. Geophys. Res. Atmos.* **120**: 7006–7024.

Xu XD, Lu CG, Shi XH, Gao ST. 2008. World water tower: An atmospheric perspective. *Geophys. Res. Lett.* **35**: L20815.

Xu XD, Lu CG, Ding YH, Shi XH, Guo YD, Zhu WH. 2013. What is the relationship between China summer precipitation and the change of apparent heat source over the Tibetan Plateau. *Atmos. Sci. Lett.* **14**: 227–234.

Yin SQ, Chen DL, Xie Y. 2009. Diurnal variations of precipitation during the warm season over China. *Int. J. Climatol.* **29**: 1154–1170.

Yu RC, Yuan WH, Li J, Fu YF. 2010. Diurnal phase of late-night against late-afternoon of stratiform and convective precipitation in summer southern contiguous China. *Clim. Dyn.* **35**: 567–576.

Yuter SE, Houze RA. 1995. 3-dimensional kinematic and microphysical evolution of Florida cumulonimbus. Part II: frequency-distributions of vertical velocity, reflectivity, and differential reflectivity. *Mon. Weather Rev.* **123**: 1941–1963.

Zhang DM, Wang ZE, Liu D. 2010. A global view of midlevel liquid-layer topped stratiform cloud distribution and phase partition from CALIPSO and CloudSat measurements. *J. Geophys. Res. Atmos.* **115**: D00H13.

Zhang DM, Luo T, Liu D, Wang ZE. 2014. Spatial scales of altocumulus clouds observed with collocated CALIPSO and CloudSat measurements. *Atmos. Res.* **149**: 58–69.

Zhong L, Su ZB, Ma YM, Salama MS, Sobrino JA. 2011. Accelerated changes of environmental conditions on the Tibetan plateau caused by climate change. *J. Clim.* **24**: 6540–6550.

Zhu YX, Liu HW, Ding YH, Zhang FY, Li W. 2015. Interdecadal variation of spring snow depth over the Tibetan Plateau and its influence on summer rainfall over East China in the recent 30 years. *Int. J. Clim.* **35**: 3654–3660.

